Mitigate the impact of ELT architecture on AO performance: learn from today´s telescopes to characterize and prevent the island effect

M. N'Diaye[1], F. Martinache[1], N. Jovanovic[2,3], J. Lozi[2], O. Guyon[2,4,5,6],
B. Norris[7], A. Ceau[1], D. Mary[1]

[1] Université Côte d´Azur, Observatoire de la Côte d´Azur, CNRS, Laboratoire Lagrange, Bd de l´Observatoire, CS 34229, 06304 Nice cedex 4, France
[2] National Astronomical Observatory of Japan, Subaru Telescope, National Institutes of Natural Sciences, Hilo, HI 96720, USA
[3] Department of Physics and Astronomy, Macquarie University, 2109 Sydney, Australia
[4] Astrobiology Center, National Institutes of Natural Sciences, 2-21-1 Osawa, Mitaka, Tokyo, Japan
[5] Steward Observatory, University of Arizona, Tucson, 933 N Cherry Ave, Tucson, AZ 85721, USA
[6] College of Optical Science, University of Arizona, 1630 E University Blvd, Tucson, AZ 85719, USA
[7] Sydney Institute for Astronomy (SIfA), School of Physics, University of Sydney, NSW 2006, Australia.

ABSTRACT

Island effects (IE) are critical piston differential aberrations between neighbouring pupil segments on ground-based telescopes that degrade the quality of Adaptive optics (AO) images on 8m-class telescopes in good observing conditions. Due to telescope architecture, these residual errors lead to a loss of observing time, up to 20% as observed on the VLT during the direct imaging observations of planetary companions with SPHERE. These effects are expected to be even more critical with ELTs as these observatories will present more complex architectures. Measuring these effects however prove very challenging for most of the state-of-the-art AO wavefront sensors. A first successful diagnosis of these aberrations has recently been obtained on SPHERE with ZELDA, the Zernike wavefront sensor for the measurement of residual aberrations in coronagraphic systems. In this communication, we focus on the Asymmetric Pupil Fourier-wavefront sensor (APF-WFS) that relies on point source images to retrieve wavefront errors with an interferometric analysis. Assuming the archetypal four-quadrant aperture geometry in 8 m class telescopes, we define aberration modes based on piston, tip, and tilt over the pupil quadrants and derive a calibration matrix for the LWE measurement in closed-loop operation with our sensor. Using the sensor mask present in Subaru/SCExAO, we perform first tests on a real system with an internal source and on sky, showing the ability of our sensor path to control these wavefront errors in the small aberration regime. Our approach looks very promising for the IE issue in the perspective of ELTs.

Keywords: telescopes, adaptive optics, high angular resolution, data analysis

1. INTRODUCTION

High-contrast observations of exoplanets and disks from the ground have been rising up for the past few years, thanks to the recent deployment of extreme adaptive optics (ExAO) with coronagraphs on 8 m class telescopes, such as the VLT/SPHERE, Gemini/GPI, or Subaru/SCExAO.[1–3] So far, these exoplanet imagers have been able to detect companions down to warm gas giant exoplanets with contrast ratio up to 10^5-10^6 at separations as low as 0.2-0.3 arcsec in the near infrared. The observation of lighter or colder companions orbiting their parent star with larger contrast ratios at smaller separations is however currently limited by several hurdles.

The main limiting factor lies in the presence of the noncommon path aberrations (NCPA) between the ExAO sensing path and the science path in the exoplanet imagers. Different solutions are already set in these instruments[4–9] and novel strategies are currently being investigated to further calibrate these errors at different spatial frequency regimes with

mamadou.ndiaye@oca.eu

accuracy.[10–13] Unfortunately, other limiting factors were unexpected at the time of instrument development, one of the most infamous being the island effect (IE)*. Such an effect comes from both: (i) good observing conditions with low-wind speed giving rise to wavefront errors with low temporal frequency and possibly amplitude larger than 1 rad, and (ii) the atmosphere producing errors with high and low temporal frequencies but small amplitude.

During ExAO observations, IE mostly appears under good seeing conditions with low-wind speeds (< 3 m/s) and is known as low-wind effect in the literature.[14] In this scenario, IE originates from the temperature exchange between the air and the telescope spiders, generating spatial discontinuities of the refractive index of the air and therefore, producing an electric field for the star that presents optical path differences between the four quadrants of the telescope pupil that are formed by the spider struts. Another downside of this effect is their slow variation in time, degrading the performance of post-processing methods for exoplanet observation and analysis. Similar wavefront discontinuities have however also been noticed during normal conditions of observations among the atmospheric turbulence aberrations at Subaru Telescope. Experienced with SCExAO, this effect appears when running the adaptive optics (AO) control loop on an internal source with strong turbulence applied to the deformable mirror (DM) of the instrument.

This spurious effect can be described as a combination of differential piston, tip, and tilt between the light in the quadrants of the telescope pupil. For the image of an unresolved star, such aberrations lead to the degradation of the star point-spread function (PSF), hence preventing coronagraphs from removing starlight efficiently. The impact of these aberrations is disastrous on science operations as they occur during the best-suited observing conditions for exoplanet imaging, leading to a significant loss of observation, up to 20% in the case of SPHERE.[14] This effect is not detected by the ExAO wavefront sensors as IE appears in the null space of the sensor response, therefore representing a challenge to overcome for its calibration.

In the exoplanet imaging context, the IE was first successfully diagnosed on SPHERE using ZELDA, a Zernike wavefront sensor to calibrate residual aberrations in coronagraphic instruments to support the main control loop of the ExAO system with an additional control loop.[12,14,15] In parallel to this concept, other sensors for NCPA calibration have been developed and implemented in analogous instruments. Among them is the Asymmetric Pupil Fourier Wavefront Sensor (APF-WFS),[11] a focal plane wavefront sensor with a prototype that is installed on SCExAO. Phase diversity methods are also emerging to accurately estimate these pupil phase discontinuities.[16]

In this communication, we investigate the calibration of the IE for small phase errors with APF-WFS and the corresponding control loop on SCExAO. We recall the principle of this focal plane wavefront sensor and detail the control loop operations using this sensor. First experimental results are presented with our concept on SCExAO under in-lab tests and on-sky observations to validate the principle. Finally, we draw preliminary conclusions and discuss their implications for further exoplanet high-contrast observations.

2. WAVEFRONT CONTROL FOR THE ISLAND EFFECT

2.1 Principle and formalism of the APF-WFS

The APF-WFS is based on the Fourier analysis of the image for an observed unresolved star to retrieve the wavefront errors in the system.[11,17] Figure 1 shows a schematic view of the APF-WFS principle. The telescope pupil can be described as a combination of subapertures by means of pupil discretization. From an interferometric standpoint, the unresolved star PSF therefore represents the result of optical interferences between all the subapertures. Performing a Fourier transform of the star image thus allows one to analyze the PSF in the Fourier plane, also known as the (u,v)-plane in interferometry. The coverage is a result of the baselines that are formed between all the interfering subapertures. This operation leads to a relation between the image plane intensity and its Fourier transform.

The phases in the image plane φ, and in the Fourier space Φ, are linearly related in the small aberration regime ($\varphi \ll 1$ rad). Using pupil discretization and in the absence of companions or disks in the astrophysical scene, this relation can be expressed as

$$\Phi = \mathbf{A}\,\varphi\,, \tag{1}$$

in which **A** denotes the transfer matrix between the two types of phase. By inverting this relation, we access the wavefront error but are left with the problem of its sign ambiguity. To lift this degeneracy, Martinache et al. (2013)[11] introduced an asymmetry in the pupil by means of a mask, leading to an unambiguous determination of the wavefront error.

As **A** is rectangular, we produce its pseudo-inverse $\mathbf{A}^+$ numerically by implementing singular value decomposition (SVD) of the original matrix. The corresponding singular values spread over several orders of magnitude and thus, the smallest values have lower impact on the phase reconstruction and can hence be set to zero without loss of too much information. By denoting k the number of first ordered singular values that are left non null, the corresponding pseudo-inverse matrix $\mathbf{A}_k^+$ leads us to an estimate of the wavefront error $\hat{\varphi}$, given by

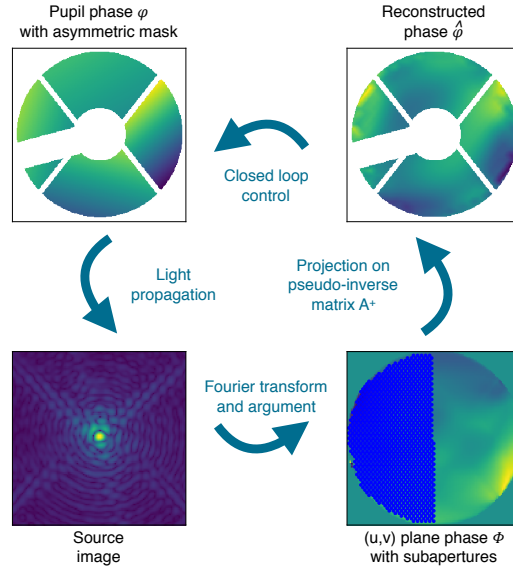$$\hat{\varphi} = \mathbf{A}_k^+ \, \Phi \,. \tag{2}$$

Figure 1. Scheme of the phase reconstruction process with APF-WFS: phase map φ within the asymmetric pupil mask (top left), source image on the camera (bottom left), phase Φ of the Fourier-plane signature in the (u,v) plane overlapped with half of the subaperture discretization (bottom right), and the reconstructed pupil phase map $\hat{\varphi}$ from the pseudo-inverse matrix $\mathbf{A}^+$ (top right).

2.2 Calibration of the island effect

The IE characterization requires defining an adequate mode basis for modal closed-loop correction. Most of the 8 m class monolithic telescopes present a pupil that splits up in four quadrants with the shadow of the secondary mirror and support struts on the primary mirror. Under this pupil geometry, the IE can be visualized as the combination of piston, tip, and tilt in each telescope pupil quadrant, i.e. the first three Zernike modes over four quadrants.

These aberrations form a natural set of 12 modes that can be represented in a vector form and gathered in a matrix. Computing the rank for this matrix leads us to a value of 11 instead of 12, showing some redundancy between the modes. We recover an 11-rank matrix by removing one of the four piston modes to form an 11-mode matrix, see Figure 2 left panel. Such an operation is useful to ensure the stability of a wavefront control algorithm.

Assuming the Subaru Telescope aperture for the pupil geometry, a closed-loop system with a DM and an APF-WFS with observation at the wavelength λ, we acquire the response of each of these 11 modes and assemble them into a response matrix **L**: we excite each mode on the DM, produce the respective PSF, retrieve the corresponding phase response from the wavefront sensing analysis, and gather the responses from the 11 modes in a matrix form. For illustration, we work in H-band at $\lambda=1.6\,\mu$m with the parameters of the APF-WFS that is used on SCExAO:[17] a discrete model containing 292 subapertures that are spaced by 0.39 m across the 7.92 m telescope pupil and a mask with an arm that is oriented with a position angle of 165° in the clockwise direction in the pupil plane and presents a thickness of 13% of the pupil diameter. By selecting one sub-aperture as a reference, we obtain a total number of 291 singular modes for this model. Figure 2 right panel displays the reconstructed phase for the 11 modes and a wavefront error of 100 nm RMS, showing good consistency with the modes introduced by the DM and represented in Figure 2 left panel.
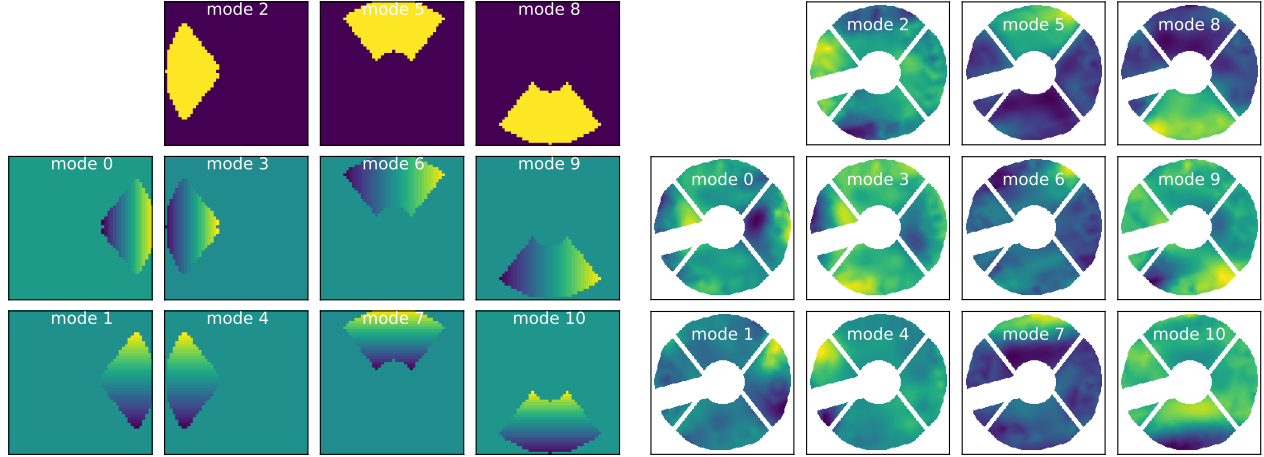
Figure 2. **Left**: Panels of the 11 modes for the DM to control the island effect. Each panel column corresponds to a pupil quadrant and panel rows correspond to piston, tip, and tilt starting from the top. **Right**: Reconstruction of the 11 IE modes with a wavefront error of 100 nm RMS, using 100 out of the 291 modes that are kept in the model. The modes are represented in the presence of the asymmetric pupil mask.

2.3 Closed-loop operation

Our goal now is to compensate for the IE in a closed-loop operation based on our calibration. A PSF is acquired in the presence of the asymmetric pupil mask and analyzed with the wavefront sensing algorithm to extract the respective phase φ. This instant wavefront is a linear combination of the 11 modes with appropriate coefficients α,

$$\varphi = \mathbf{L}\,\alpha. \tag{3}$$

The coefficients α can be estimated by minimizing $\|\varphi - \mathbf{L}\alpha\|^2$. Resolving this least-square problem provides us coefficients $\hat{\alpha}$ that are associated with the 11 modes to produce a map to apply to the DM and perform modal control:

$$\hat{\alpha} = \mathbf{L}^+\,\varphi\,, \tag{4}$$

with $\mathbf{L}^+ = (\mathbf{L^T\,L})^{-1}\,\mathbf{L^T}$. In a real-life system, a control loop gain smaller than 1 is used to ensure its convergence towards a null wavefront error with the control algorithm.

At this point, it is interesting to compare the IE maps resulting from this experimental process and from the product $\mathbf{A}^+\mathbf{A}$ from the combination of Eqs. (1) and (2) to determine the quality of the map reconstruction. We first generate a phase map with a linear combination of the 11 modes, using the coefficients given in Table 1. Our simulations are made in the absence of noise (no shot noise nor readout noise). Figure 3 shows the initial map in the left panel and the maps resulting from both reconstruction methods in the middle and right panels. For the experimental case, we use a cutoff $k = 100$ for the singular modes of the model, relying on previous APF-WFS works with Zernike modes.[11,17] The reconstructed map in the right panel from the experiment through image processing, is visually similar to the ideal reconstruction from the product $\mathbf{A}^+\mathbf{A}$ in the middle panel. Though they are mostly qualitative, these results are encouraging in terms of quality of the wavefront reconstitution with respect to the theoretical case for the IE modes. On-going studies will allow us to assess the quality of the results quantitatively and find the optimal mode cutoff for phase reconstruction.

Table 1. Amplitude of the modes in wavefront errors to produce the arbitrary IE map used in our simulations, assuming observation in H-band ($\lambda = 1.6\,\mu$m).

modes	0	1	2	3	4	5	6	7	8	9	10
RMS (nm)	-26	100	30	-26	20	34	-16	18	-4	24	30

3. FIRST TESTS ON SCEXAO

We now use the APF-WFS with Subaru/SCExAO to demonstrate its capability to compensate for the IE on a real instrument. Our experiments are first led with the internal source and then on sky with the light coming from the Subaru
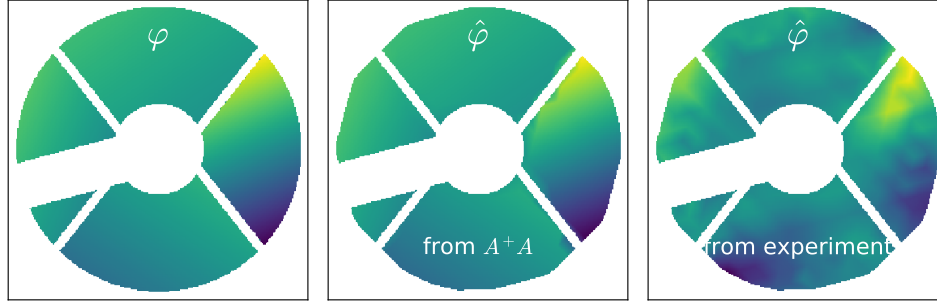
Figure 3. From left: initial IE map φ, reconstructed phase map $\hat{\varphi}$ from the linear model with $\mathbf{A}^+\mathbf{A}$ and no cutoff, and reconstructed phase map $\hat{\varphi}$ from the experimental process with the linear model and a cutoff of singular modes $k = 100$.

Telescope combined with the adaptive optics system AO188.

3.1 Integration on a real system

We briefly review the relevant features of the instrument for our tests. A more complete description of SCExAO and its capabilities can be found in the literature.[3]

SCExAO relies on several control loops to measure wavefront error contributions in different spatial frequency regimes and correct for them with a 2000-actuator DM (45 actuators across the pupil diameter). These loops involve the two instrument channels: (1) a visible channel containing the main loop with a pyramid wavefront sensor to calibrate the atmospheric turbulence and (2) a near-infrared channel including an arm with the Lyot-based low-order wavefront sensor[7] and an InGaAs CMOS science camera in the final image plane for PSF acquisition. The visible channel also includes VAMPIRES, a module based on non-redundant aperture masking interferometry[18] and differential polarimetry to image the innermost regions of protoplanetary disks.[19] Its camera relies on a 512x512 pixel EMCCD detector with $16\,\mu$m pixel size. In the near-infrared channel, the camera is based on a 320x256 pixel size detector with a $30\,\mu$m pixel size and acquires images at a $170\,$Hz frame rate with a $140\,\mathrm{e}^-$ RMS readout noise. Pupil imaging is made possible by inserting a lens in front of the camera and translating the conjugation of the camera to a pupil plane. The near-infrared channel also includes a filter wheel with an asymmetric pupil mask in a plane that is conjugated to the telescope pupil plane, enabling APF-WFS measurements with the CMOS camera.

Every control loop sensor or corrector has a set of basis modes to control the corresponding device. In previous work,[17] a Zernike basis set of modes was used for the APF-WFS to measure the residual low-order aberrations in the system. This basis however does not encompass the IE modes to calibrate. We here use an orthogonalized set of IE modes that are shown in Figure 4 left panel to evaluate the calibration of the differential piston effects and the simultaneous correction of mixed modes.

For our tests with the asymmetric pupil mask, we keep the pupil model with 292 subapertures from Martinache et al. (2016).[17] Unless otherwise stated, we keep the first 100 model singular modes for the phase reconstruction and for each experiment configuration, we acquire 100 images in H-band with a $10\,\mu$s integration time. These images are then dark subtracted, recentered, and finally stacked together to produce a final averaged image.

3.2 In-lab results with the internal source

We first perform tests with the internal source to validate our focal plane wavefront sensor for the IE measurements in the laboratory. We study our concept with the analysis of its response to the 11 IE modes and we operate it in closed-loop operation for the control of a given IE phase map. A control loop gain of 0.05 was used.

3.2.1 Sensor response to IE modes

Figure 4 right panel shows the H-band PSFs resulting from the introduction of each of the 11 orthogonalized modes on the DM with $50\,$nm RMS amplitude, i.e. $100\,$nm RMS wavefront error. Although quite similar at first glance, small differences can be seen by inspecting the first diffraction ring and the speckle field at larger angular separations. Such a set of images was later used to perform the APF-WFS modal calibration step before operating wavefront control. These images are
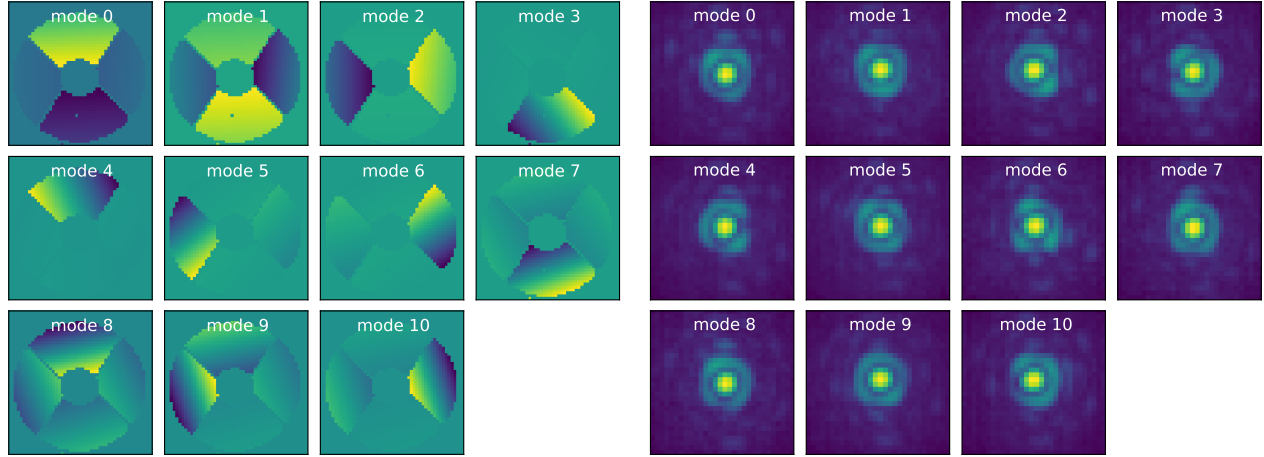
Figure 4. **Left**: Display of the 11 modes for the DM to control the island effect on SCExAO. These modes represent an orthogonalized version of the modes that are shown in Figure 2 left panel. They include the dead actuator of the SCExAO DM that is visible in the bottom quadrant of the pupil, for a few of these modes. **Right**: PSFs for the 11 modes on the left panel with $100\,\text{nm}$ RMS wavefront error, in the presence of the asymmetric pupil mask.

acquired at a single excitation amplitude. In a forthcoming paper, we will analyze the sensor response to a wide range of excitations to provide a broader description of the sensor behavior.

3.2.2 Wavefront control loop

After the modal calibration step, we investigate closed-loop wavefront control using the APF-WFS for an arbitrary IE phase map. Figure 5 shows the evolution of the PSF over time. As a first step, we work with SCExAO using the DM with a shape that compensates for the aberrations from its curvature at rest, providing a clean PSF on the camera. A few seconds later, we introduce the IE map on the DM and observe a degraded PSF on the camera. Another ten seconds later, we close the control loop and observe a rapid convergence, enabling a good quality recovery of the initial PSF. These qualitative results already looks promising for the correction of IE mode. They will further be completed with an analysis of the temporal evolution of the wavefront error.
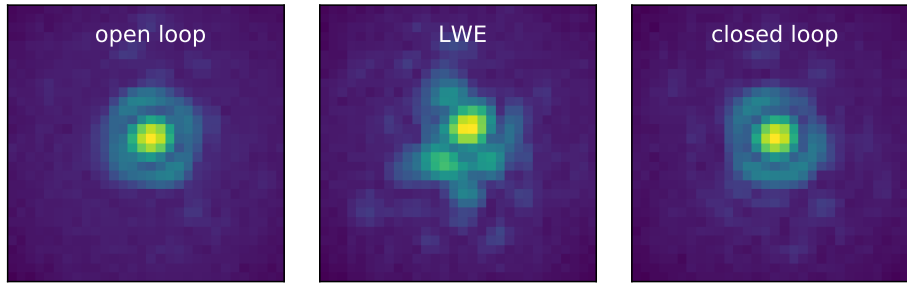

Figure 5. H-band images at different steps of the experiment from left: in open loop without IE, after introduction of the IE on the DM, and after closed-loop wavefront control. The initial and final PSFs exhibit similar clean structures.

3.3 First on-sky demonstration

After tests with an internal source, we operate our closed-loop wavefront control for on-sky demonstration with an un-resolved bright star, Procyon A. Our acquisitions were obtained on Subaru Telescope during the SCExAO run on UT 2017-03-12 over a one hour time period. A 3.2 m/s wind speed and a 0.45 arcsec seeing at $0.5\,\mu\text{m}$ were noted, corresponding to good observing conditions. We tested our wavefront control loop based on APF-WFS measurements for the

compensation of the IE and we evaluated the quality of the correction based on image acquisition with the IR and visible SCExAO benches: (i) in the near-infrared at $1.6\,\mu$m (H-band) using the CMOS science camera and (ii) in visible light at 750 nm with the VAMPIRES module relying on its EMCCD camera.[19] As a reminder, the control loop works in the near infrared.

We first observe our star image in open loop in H-band and notice a well-structured PSF, resulting from the good observing conditions during our run and the small IE amount present during our tests. Closing our control loop therefore does not show any major improvement in the PSF quality. Following our experiment in the near-infrared, we repeat the observations in the visible. As AO efficiency decreases at shorter wavelengths, there are more uncorrected aberrations in shorter wavebands, leading to an image quality in the visible that is worse than in the near-infrared. Despite this known issue, we operate our wavefront control loop and analyze our VAMPIRES images, see Figure 6. Our PSFs show sharpness differences in open and closed-loop corresponding to a visual improvement in resolution. Quantitatively, we estimate the Strehl ratio by measuring the PSF intensity peak in the images and find a relative increase by 37% between the images before and after closing the loop. Such an improvement only results from the IE correction that is achieved with our wavefront control loop. Although mostly qualitative, these first results prove very encouraging in terms of IE compensation on images in the visible. Obviously, further tests are required to evaluate in a quantitative way and confirm the efficiency of our algorithm for the IE in the near infrared. However, these preliminary results already underline the ability of our algorithm based on APF-WFS measurements to compensate for the IE on sky.
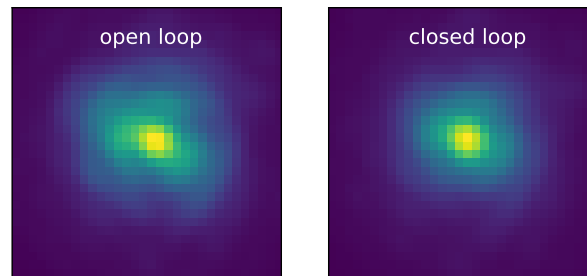

Figure 6. SCExAO/VAMPIRES images of Procyon A at 750 nm before (left) and after (right) our focal plane closed-loop wavefront control on the IE. A 0.5 power scale is used to represent these frames. The star image is sharper after IE compensation.

4. CONCLUSION

Mostly appearing at the time of the best observing conditions, the IE results in spurious and uncontrolled aberrations that strongly limit the detection of exoplanets by direct imaging. In this paper, we present preliminary results for the calibration of the IE with a focal plane wavefront control algorithm based on APF-WFS measurements in the small aberration regime. We experimentally test our control loop with Subaru/SCExAO on the internal source and on sky. Qualitatively, preliminary testing shows image quality improvement in laboratory and on sky, proving very promising in the context of exoplanet high-contrast observations. Quantitatively, we will complete our study in a forthcoming paper to estimate the performance and current limits of our focal plane wavefront control loop.

The gained experience from the calibration of this unexpected effect will help the community to face unforeseen aberrations with the ELTs that exhibit a more complex architecture than the current 8 m class telescopes and to develop wavefront control algorithms that will efficiently address unknown artifacts. In exoplanet imagery, addressing such critical aspects will rapidly bring important benefits to future observatories with an increased capability in studying exoplanets that are fainter or closer to their host stars than the current substellar mass companions and further complete the exoplanet landscape at different age, mass, orbit, and nature.

REFERENCES

[1] Beuzit, J., Feldt, M., Dohlen, K., et al., "SPHERE: a planet finder instrument for the VLT," in [*SPIE*], **7014** (Aug. 2008).

[2] Macintosh, B. A., Graham, J. R., Palmer, D. W., et al., "The Gemini Planet Imager: from science to design to construction," in [*Society of Photo-Optical Instrumentation Engineers (SPIE) Conference Series*], **7015** (July 2008).

[3] Jovanovic, N., Martinache, F., Guyon, O., et al., "The Subaru Coronagraphic Extreme Adaptive Optics System: Enabling High-Contrast Imaging on Solar-System Scales," *PASP* **127**, 890 (Sept. 2015).

[4] Baudoz, P., Dorn, R. J., Lizon, J.-L., et al., "The differential tip-tilt sensor of SPHERE," in [*Ground-based and Airborne Instrumentation for Astronomy III*], *Proc. SPIE* **7735**, 77355B (July 2010).

[5] Savransky, D., Thomas, S. J., Poyneer, L. A., and Macintosh, B. A., "Computer vision applications for coronagraphic optical alignment and image processing," *Applied Optics* **52**, 3394 (May 2013).

[6] Huby, E., Baudoz, P., Mawet, D., and Absil, O., "Post-coronagraphic tip-tilt sensing for vortex phase masks: The QACITS technique," *A&A* **584**, A74 (Dec. 2015).

[7] Singh, G., Lozi, J., Guyon, O., et al., "On-Sky Demonstration of Low-Order Wavefront Sensing and Control with Focal Plane Phase Mask Coronagraphs," *PASP* **127**, 857 (Sept. 2015).

[8] Sauvage, J.-F., Fusco, T., Rousset, G., and Petit, C., "Calibration and precompensation of noncommon path aberrations for extreme adaptive optics," *Journal of the Optical Society of America A* **24**, 2334–2346 (Aug. 2007).

[9] Wallace, J. K., Burruss, R. S., Bartos, R. D., et al., "The Gemini Planet Imager calibration wavefront sensor instrument," in [*Society of Photo-Optical Instrumentation Engineers (SPIE) Conference Series*], **7736** (July 2010).

[10] Galicher, R., Baudoz, P., Rousset, G., Totems, J., and Mas, M., "Self-coherent camera as a focal plane wavefront sensor: simulations," *A&A* **509**, A31 (Jan. 2010).

[11] Martinache, F., "The Asymmetric Pupil Fourier Wavefront Sensor," *PASP* **125**, 422–430 (Apr. 2013).

[12] N'Diaye, M., Dohlen, K., Fusco, T., and Paul, B., "Calibration of quasi-static aberrations in exoplanet direct-imaging instruments with a Zernike phase-mask sensor," *A&A* **555**, A94 (July 2013).

[13] Paul, B., Sauvage, J.-F., and Mugnier, L. M., "Coronagraphic phase diversity: performance study and laboratory demonstration," *A&A* **552**, A48 (Apr. 2013).

[14] Sauvage, J.-F., Fusco, T., Lamb, M., et al., "Tackling down the low wind effect on SPHERE instrument," in [*Society of Photo-Optical Instrumentation Engineers (SPIE) Conference Series*], *Proc. SPIE* **9909**, 990916 (July 2016).

[15] N'Diaye, M., Vigan, A., Dohlen, K., et al., "Calibration of quasi-static aberrations in exoplanet direct-imaging instruments with a Zernike phase-mask sensor. II. Concept validation with ZELDA on VLT/SPHERE," *A&A* **592**, A79 (Aug. 2016).

[16] Lamb, M., Correia, C., Sauvage, J.-F., et al., "Quantifying telescope phase discontinuities external to AO-systems by use of Phase Diversity and Focal Plane Sharpening," *ArXiv e-prints* (July 2017).

[17] Martinache, F., Jovanovic, N., and Guyon, O., "Closed-loop focal plane wavefront control with the SCExAO instrument," *A&A* **593**, A33 (Sept. 2016).

[18] Tuthill, P. G., Monnier, J. D., Danchi, W. C., Wishnow, E. H., and Haniff, C. A., "Michelson Interferometry with the Keck I Telescope," *PASP* **112**, 555–565 (Apr. 2000).

[19] Norris, B., Schworer, G., Tuthill, P., et al., "The VAMPIRES instrument: imaging the innermost regions of protoplanetary discs with polarimetric interferometry," *MNRAS* **447**, 2894–2906 (Mar. 2015).

[20] Couder, A., "Sur un Effet Thermique: Observé dans les Télescopes a Réflexion," *L'Astronomie* **63**, 253–258 (1949).